
EXAONE Path 2.5: Pathology Foundation Model with Multi-Omics Alignment

Juseung Yun Sunwoo Yu Sumin Ha Jonghyun Kim
 Janghyeon Lee Jongseong Jang Soonyoung Lee
 LG AI Research

Abstract

Cancer progression arises from interactions across multiple biological layers, especially beyond morphological and across molecular layers that remain invisible to image-only models. To capture this broader biological landscape, we present EXAONE Path 2.5, a pathology foundation model that jointly models histologic, genomic, epigenetic and transcriptomic modalities, producing an integrated patient representation that reflects tumor biology more comprehensively. Our approach incorporates three key components: (1) multimodal SigLIP loss enabling all-pairwise contrastive learning across heterogeneous modalities, (2) a fragment-aware rotary positional encoding (F-RoPE) module that preserves spatial structure and tissue-fragment topology in WSI, and (3) domain-specialized internal foundation models for both WSI and RNA-seq to provide biologically grounded embeddings for robust multimodal alignment. We evaluate EXAONE Path 2.5 against six leading pathology foundation models across two complementary benchmarks: an internal real-world clinical dataset and the Patho-Bench benchmark covering 80 tasks. Our framework demonstrates high data and parameter efficiency, achieving on-par performance with state-of-the-art foundation models on Patho-Bench while exhibiting the highest adaptability in the internal clinical setting. These results highlight the value of biologically informed multimodal design and underscore the potential of integrated genotype-to-phenotype modeling for next-generation precision oncology.

1 Introduction

The rapid advancement of computational pathology has unlocked new avenues for understanding cancer biology through large-scale digital image analysis [2, 3, 4, 8]. Whole-slide images (WSI) now serve as powerful representations of tumor morphology, capturing spatial phenotypes across the heterogenous tissue region using self-supervised learning frameworks [5, 16, 21, 28, 29, 30]. However, morphology alone remains insufficient for explaining disease mechanisms, as it does not directly reveal the genetic, epigenetic, and transcriptional alterations driving tumor progression [9].

To this end, recent studies have begun incorporating spatial transcriptomics or pathology reports to enrich WSI-derived representations [6, 15, 23, 26]. Building on this direction, we propose a multimodal framework that jointly integrates five complementary molecular and histopathologic modalities: **WSI, bulk RNA-seq, single-nucleotide polymorphisms (SNP), copy-number variations (CNV), and DNA methylation**. Each modality captures a different layer of tumor biology, and their unified modeling provides a more complete and biologically grounded patient representation [10, 12]. By constructing a shared latent space spanning genomic, epigenetic, transcriptomic, and phenotypic dimensions, we aim to move toward explainable multimodal oncology.

Although these modalities are correlated, they encode largely orthogonal biological signals. SNPs and CNVs describe the genomic alterations initiating or promoting tumorigenesis [14, 24]. These changes

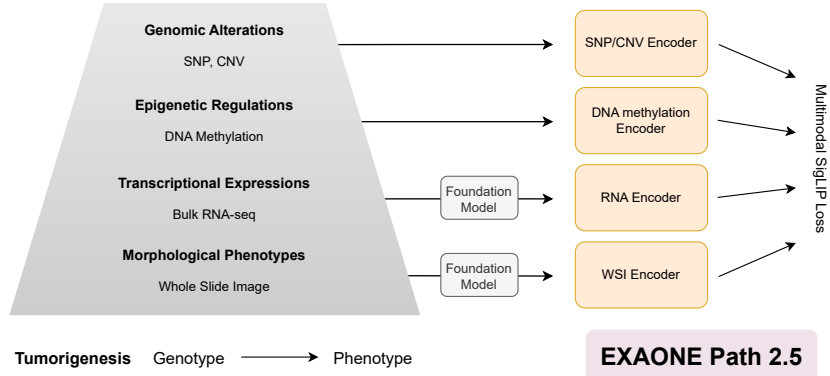


Figure 1: Overall scheme of EXAONE Path 2.5. Whole-slide images are aligned with multi-omics data using a multimodal SigLIP loss that enables all-pairwise cross-modal alignment. By jointly modeling multiple layers of tumor biology from genotype to phenotype, our model produces biologically enriched histopathology representations.

often shape epigenetic regulation through DNA methylation [18], which in turn modulates transcriptional programs observed in bulk RNA-seq [22]. WSI then captures the macroscopic phenotype that emerges from these molecular processes. Integrating these five layers of tumorigenesis—from genotype to phenotype—offers a comprehensive view of cancer that cannot be achieved by any single modality alone [7].

To realize this integration, we design a *pathology-oriented multimodal alignment framework* tailored to real-world clinical variability and missing-modality patterns.

- **Multimodal SigLIP Loss:** We propose a modified SigLIP contrastive loss [31] to support efficient *all-pairwise contrastive learning* across the five modalities. All modality pairs are projected using its respective adapter, allowing them to capture different semantic aspects of importance to another modality. This objective encourages each modality to encode complementary biological information while preventing collapse toward any single, easier modality.
- **Fragment-Aware Rotary Position Encoding:** Instead of treating WSI features as unordered tile sets, we preserve spatial structure by *rotary positional embeddings with fragment-aware attention masking*. This allows the model to differentiate distinct tissue fragments on a slide and capture region-level histologic patterns (e.g., variations in tumor grade, stromal composition, or immune infiltration) that often reflect underlying molecular states.
- **Internal Foundation Models for WSI and RNA-seq:** We leverage *internal foundation models* that were pretrained on histopathology and transcriptomic datasets independently. These domain-specialized foundation models provide stable, biologically meaningful embeddings that improve both the robustness and effectiveness of multimodal contrastive alignment.

This domain informed design yields strong resource efficiency, enabling the model to match or surpass state-of-the-art performance across diverse tasks with substantially fewer training samples and parameters.

2 Methods

2.1 Multimodal SigLIP Loss

Standard CLIP-based losses assume that there is only one correct positive per row. As the softmax function forces all probabilities in a row to sum to 1, the presence of multiple valid positive modalities leads to competition between positives. To avoid this limitation, we adopt the sigmoid-based binary cross-entropy (BCE) loss from SigLIP [31], which treats every pair in the similarity matrix as an independent binary classification problem. We extend this SigLIP formulation to our multimodal setting with M modalities.

For each sample n , we form an $M \times M$ block of modality–modality relationships. $\mathbf{x}_{n,i} \in \mathbb{R}^C$ denotes the feature of modality i for sample n . For every possible modality pair (i, j) , we associate a dedicated projection parameterized by a weight matrix $\mathbf{W}_{i,j} \in \mathbb{R}^{C \times C}$ and a bias vector $\mathbf{b}_{i,j} \in \mathbb{R}^C$. The projected embedding from modality i to modality j is computed as

$$\mathbf{h}_{n,i \rightarrow j} = \text{Normalize}(\mathbf{W}_{i,j} \mathbf{x}_{n,i} + \mathbf{b}_{i,j}).$$

Projecting each source modality into the representational space of every target modality enables the model to learn modality-pair-specific interaction spaces between biological layers. Similarities are computed across the global batch, yielding modality-pair-specific logits

$$\ell_{n,i,k,j} = \alpha_{i,j} \cdot \langle \mathbf{h}_{n,i \rightarrow j}, \mathbf{h}_{k,j \rightarrow i} \rangle + \beta_{i,j},$$

where $\alpha_{i,j}$ and bias $\beta_{i,j}$ are learnable modality-dependent scaling and bias parameters. Each logit is then compared against a binary target $t_{n,i,k,j} \in \{0, 1\}$ indicating whether modality i of sample n forms a valid positive pair with modality j of sample k :

$$t_{n,i,k,j} = \mathbf{1}(n \equiv k) \times \text{ValidPair}_{n,i,j},$$

where $\text{ValidPair}_{n,i,j}$ denotes whether modalities i, j are both available for sample n . Positives occur only within the same sample while negatives are collected across the global batch. The loss for each modality pair is computed as

$$\mathcal{L}_{n,i,k,j} = \text{BCEWithLogits}(\ell_{n,i,k,j}, t_{n,i,k,j}).$$

Overall, our modified Multimodal SigLIP loss allows every modality pair (i, j) to contribute to an independent BCE term, with class balancing achieved by averaging positive and negative contributions.

2.2 Fragment-Aware Rotary Position Encoding (F-RoPE)

High resolution whole-slide images are typically processed as a set of local patches. While patch-level encoders capture local morphology, naively aggregating these features ignores the spatial organization of tissue and may blur biologically meaningful structures. At the same time, multiple separated regions on a single slide are common in routine histopathology workflows, where several tissue sections from the same patient (e.g., different biopsy site, stain type) are stained together [1, 17]. Hence, F-RoPE aims to consider the decomposition of slides into separate tissue fragments.

To encode spatial relationships between patches while avoiding spurious positional coupling across physically disconnected regions, we augment the WSI aggregator with (1) RoPE-based positional encoding [25] and (2) a fragment-aware attention mask. For each patch, we maintain its pixel coordinate and the fragment index obtained from tissue segmentation. Pixel coordinates are converted into continuous patch indices by normalizing with respect to the patch size, and then passed through a RoPE module to obtain sinusoidal position embeddings that rotate query/key vectors.

In parallel, we construct a pairwise attention mask over all tokens. Each patch token is assigned its corresponding fragment index, whereas the CLS and register tokens are grouped together and assigned to a separate single fragment. Based on this fragment index, we define a boolean mask by the equality of these indices. Then this fragment-aware mask is used to restrict attention in the RoPE branch to preserve only interactions within the fragment and suppress positional attention across disconnected tissue fragments.

Our aggregator transformer interleaves RoPE-attention and NoPE-attention blocks. The RoPE blocks incorporate rotary positional embeddings together with the fragment-aware attention mask to capture local spatial geometry and fragment-level topology. In contrast, the NoPE blocks remain fully position-agnostic over valid tokens relying solely on the padding masks. This alternating dual-attention scheme enables the model to learn both localized structural cues and global slide-level evidence without spatial bias, achieving a balanced and expressive WSI representation.

2.3 Overall Architecture: EXAONE Path 2.5

WSI Encoder. The WSI encoder E_{WSI} consists of (1) an internally pretrained WSI patch-level foundation model, (2) a Transformer-based aggregator equipped with F-RoPE, and (3) a linear projection head. WSIs are first encoded into patch embeddings using the WSI foundation model. These patch tokens are then processed with its patch coordinates through the aggregator module. The spatial fragment indices refine the final slide embedding to encompass fragment-level structural consistency.

Gene Encoders. We assign four separate gene encoders (E_{RNA} , E_{SNP} , E_{CNV} , E_{Meth}) to individually process each gene modality showing different degrees of sparsity and expressivity. RNA expression profiles are encoded using an internally pretrained RNA-seq foundation model, whereas SNP, CNV, DNA methylation expression values are encoded as fixed-length vector representations. Each encoder is a feed-forward module composed of an initial linear projection followed by several pre-norm SwiGLU FFN residual blocks.

Multimodal Embedding and Alignment. The final embeddings from all modalities are aligned using the Multimodal SigLIP loss (Section 2.1), which supervises all modality pairs jointly. This pairwise alignment formulation encourages biologically meaningful cross-modal consistency while preserving modality-specific representations in a shared embedding space.

3 Experiments

3.1 Training Data

Our multimodal training cohort consists of five complementary data modalities: whole-slide images, bulk RNA sequencing, single-nucleotide polymorphisms, copy-number variations, and DNA methylation profiles. We have curated a total of 23,099 patients who have at least two modalities available. The final dataset used to train our multimodal contrastive learning framework and WSI feature aggregator includes 23,099 WSI slides (one per patient), 29,876 RNA-seq samples, 10,250 SNP samples, 10,601 CNV samples, and 10,503 DNA methylation samples. The WSI and RNA foundation models are pretrained and used to extract patch-level and RNA-sequence embeddings while kept frozen throughout this process.

3.2 Benchmarks

To assess both real-world performance and generalizability, we evaluate our model using (1) internal clinical datasets collected from multiple hospitals and (2) the public Patho-Bench¹ benchmark suite.

(1) Internal Clinical Benchmarks. We have curated internal datasets from one general hospital in Korea (KOR) and two general hospitals in the United States (USA1, USA2). LUAD-TMB task predicts tumor mutation burden (TMB) status (high vs. low) defined according to the number of mutations per megabase with a threshold of 10 from lung adenocarcinoma (LUAD) patients. LUAD-EGFR and LUAD-KRAS identifies the presence of actionable EGFR and KRAS mutations in LUAD respectively. CRC-MSI task classifies microsatellite instability (MSI) status in colorectal adenocarcinoma (CRC). All tasks are binary classification tasks. These seven internal benchmarks evaluate cross-institution generalization clinical robustness of the learned WSI representations to transfer to real-world diagnostic and molecular prediction tasks. All data usage has been approved by the respective Institutional Review Boards (IRBs) and fully de-identified. The dataset is restricted for internal research use.

(2) Public Benchmark: Patho-Bench. We further evaluate all models on Patho-Bench, a large-scale and comprehensive benchmark suite for computational pathology. Patho-Bench spans across seven major clinical and biological task families: morphological subtyping, tumor microenvironment (TME) characterization, tumor grading, molecular subtyping, mutation prediction, treatment response prediction, and survival prediction. The dataset provides task-specific labels across diverse cancer types, enabling unified and systematic evaluation of WSI representation learning methods.

The Patho-Bench tasks utilized in our evaluation setting after excluding unavailable or corrupted datasets are shown in Table 2 and Table 4. For all experiments, we strictly follow the official 5-fold/50-fold cross-validation protocol provided by Patho-Bench. Each task includes predefined train/test splits, ensuring fair and consistent comparison with prior works. Performance is reported as the average across folds for each task, and all metrics are computed using the official evaluation scripts provided in THREADS [26].

¹ <https://huggingface.co/datasets/MahmoodLab/Patho-Bench>

Table 1: Internal Clinical Benchmark - Train : Test Split.

Task	Train (KOR)	Test (USA1)	Test (USA2)	Test (KOR)
LUAD-TMB (high : low)	1063 : 287	137 : 117	308 : 207	-
LUAD-EGFR (wild : mut)	1145 : 205	242 : 12	426 : 89	-
LUAD-KRAS (wild : mut)	1217 : 133	163 : 91	347 : 168	-
CRC-MSI (stable : instable)	2630 : 831	-	-	658 : 209

Table 2: Distribution of evaluation tasks in Patho-Bench.

Task Category	# Tasks
Mutation prediction	30
Tumor grading	7
Tumor microenvironment (TME) characterization	14
Treatment response and assessment	7
Molecular subtyping	7
Morphological subtyping	6
Survival analysis	9
Total	80

3.3 Baseline Models

We compare our method against six state-of-the-art pathology and multimodal foundation models with publicly available checkpoints. For all baselines, we adopt their official preprocessing pipelines and evaluate the released encoders without any additional fine-tuning.

UniModal Foundation Models. CHIEF [29] is a contrastive pathology foundation model pre-trained on 60K whole-slide images (WSIs) using a CTransPath [28] backbone coupled with an ABMIL [11] aggregator. Prov-GigaPath [30] is trained on 171K slides from the Prov-Path dataset using a DINOv2 [20] objective with a ViT-G backbone. We additionally include two patch-level encoders that do not provide slide-level representations. H-optimus-0² is a ViT-based encoder trained on over 500K WSIs and UNI [5] is a large-scale self-supervised model pretrained on more than 100 million WSIs.

Multimodal Foundation Models. TITAN [6] adopts a teacher–student self-distillation framework built on the pretrained CONCHv1.5³ encoder and is trained on its internal MASS-340K dataset comprising WSIs, generated region level captions and pathology reports. PRISM [23] also integrates WSIs and pathology reports using a Perceiver architecture [13] combined with the Virchow [27] pathology encoder.

3.4 Evaluation Protocols

Internal Clinical Benchmarks. For patch-level foundation models (H-optimus-0, UNI-2h), we follow UNI [5] and obtain slide-level representations using a CLAM aggregator [19]. For slide-level foundation models (CHIEF, GigaPath, PRISM, TITAN), we train a linear classifier on top of their frozen slide-level embeddings. EXAONEPath 2.5 is compared in both evaluation settings. We perform a learning-rate search and report the averaged AUROC across four random seed runs, selecting the best-performing learning rate for each model. All models are trained and evaluated using the predefined dataset splits shown in Table 1.

Patho-Bench Classification Tasks. We evaluate patch-level foundation models using mean pooling of patch embeddings followed by a linear classifier. For slide-level foundation models, we directly train a linear classifier on their released slide-level embeddings. Linear probing follows the logistic

² <https://huggingface.co/bioptimus/H-optimus-0>

³ https://huggingface.co/MahmoodLab/conchv1_5

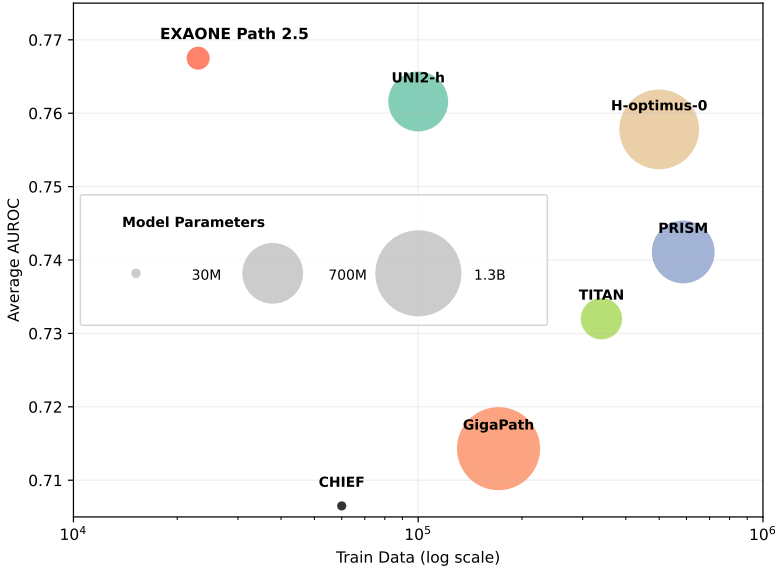


Figure 2: Internal benchmark performance of pathology foundation models. Marker area is proportional to each model’s parameter count, and the x -axis shows the pretraining data scale (log). EXAONE Path 2.5 (CLAM) delivers the best AUROC while being among the smallest models trained on the least data, outperforming billion-parameter models pretrained on substantially larger datasets.

regression configuration used in THREADS with fixed hyperparameters [26]. All classification tasks are evaluated using macro-averaged AUROC (one-vs-rest).

Patho-Bench Time-to-Event Prediction Tasks. We evaluate both patch-level and slide-level foundation models using a unified survival-probing framework. For slide-level models, we directly feed their released slide embeddings into a Cox proportional hazards model. For patch-level models, we first construct slide representations by mean pooling of patch embeddings and then train a Cox model on the resulting slide features. All Cox models use the same fixed hyperparameters as in THREADS, and performance is evaluated using the concordance index (C-index).

4 Results

4.1 Performance on Internal Clinical Benchmarks

We evaluate EXAONE Path 2.5 on internal multi-institutional benchmarks covering three lung adenocarcinoma tasks (TMB10, EGFR, KRAS) and one colorectal MSI task, each assessed across the Korean (KOR) cohort and two U.S. hospital cohorts (USA1, USA2). Table 3 reports AUROC performance against six representative pathology foundation models: TITAN, PRISM, CHIEF, GigaPath, UNI2-h, and H-optimus-0.

EXAONE Path 2.5 achieves the highest average AUROC (0.7675) across all tasks, demonstrating robust generalization under both evaluation protocols. As described in Section 3.4, slide-level foundation models (blue) are evaluated with a linear classifier, whereas patch-level models (red) require CLAM-based aggregation prior to classification. EXAONE Path 2.5 was assessed in both settings and consistently ranked first within each protocol.

Figure 2 further characterizes performance with respect to pretraining data scale and model size. Despite having substantially fewer parameters and being pretrained on less data than billion-parameter baselines, EXAONE Path 2.5 achieves superior AUROC. This highlights that architectural choices tailored to pathology—such as fragment-aware positional encoding and multimodal alignment throughout multiple biological layers—can provide greater gains than scale alone, yielding efficient and effective slide representations.

Table 3: Performance comparison across tasks and datasets. Blue cells correspond to models evaluated in the linear setting, while red cells correspond to the CLAM setting. EXAONE Path 2.5 is evaluated in both settings, and each of its configurations (linear and CLAM) achieves the best performance within its respective evaluation regime. Row-wise best values are shown in bold.

Cancer	Target	Test set	TITAN	PRISM	CHIEF	GigaPath	UNI2-h	H-optimus-0	EXAONE Path 2.5
LUAD	TMB10	USA1	0.6897	0.6664	0.6505	0.6765	0.6893	0.6590	0.6936 0.6824
		USA2	0.6904	0.6857	0.6546	0.6731	0.6860	0.6928	0.7077 0.6951
	EGFR	USA1	0.7839	0.8296	0.8109	0.7073	0.8192	0.8508	0.7843 0.8555
		USA2	0.8278	0.8163	0.7690	0.7629	0.8628	0.8535	0.8274 0.8482
		USA1	0.5895	0.5749	0.5422	0.6167	0.6075	0.5995	0.5534 0.6022
	KRAS	USA2	0.6104	0.6796	0.5987	0.6149	0.6856	0.6382	0.6983 0.7102
CRC	MSI	KOR	0.9320	0.9352	0.9199	0.9499	0.9807	0.9907	0.9609 0.9791
AVERAGE			0.7320	0.7411	0.7065	0.7143	0.7616	0.7578	0.7465 0.7675

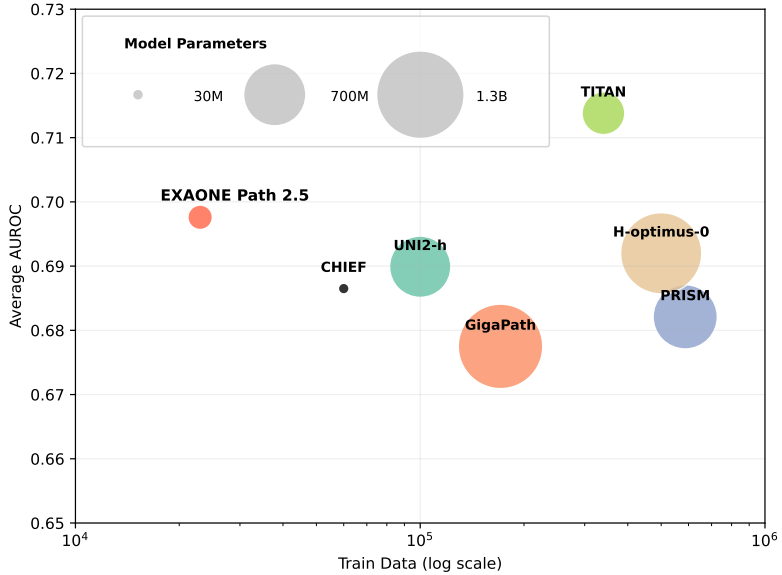


Figure 3: Performance of pathology foundation models on Patho-Bench. The plot shows average AUROC on Patho-Bench consisting of 80 tasks (5/50 fold evaluation). While prior state-of-the-art models benefit from large-scale training corpora, EXAONE Path 2.5 delivers comparable performance under a substantially smaller training regime, demonstrating favorable data–performance trade-offs.

4.2 Performance on Patho-Bench

To measure the comprehensive capability of foundation models and ensure reproducible results, EXAONE Path 2.5 is evaluated using Patho-Bench evaluation protocol. The Patho-Bench evaluation includes 26 public datasets composed of 24,483 WSIs and covers 80 tasks. Experiments are conducted with consistent settings across all baseline models. For patch-level foundation models, we apply mean pooling to aggregate features for fair comparison with slide-level approaches.

Despite substantial differences in training data scale and model size, EXAONE Path 2.5 performs on par with state-of-the-art models on Patho-Bench. EXAONE Path 2.5 demonstrates not only superior performance on out-of-distribution data but also stable and comprehensive performance across in-distribution evaluations.

To investigate how multi-omics alignment enhances the biological expressiveness of histopathology representations, we analyze the intrinsic structure of learned patch embeddings through unsupervised clustering. Specifically, (1) patch embeddings directly extracted from the internally pretrained WSI foundation model and (2) patch embeddings obtained after multimodal alignment with molecular

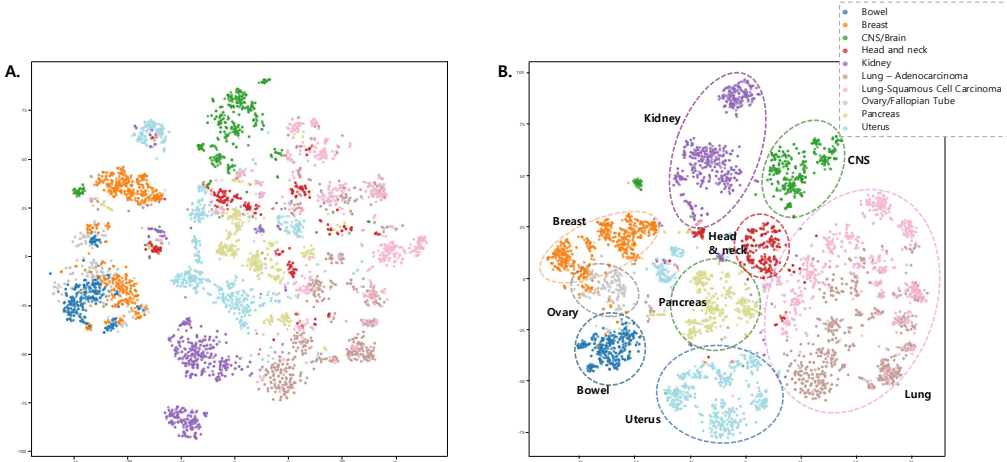


Figure 4: (A) t-SNE embedding of slide-level WSI patch features derived from the internal pathology foundation model. (B) t-SNE embedding of the same samples after cross-modal alignment with molecular features (RNA-seq, SNP, CNV, DNA methylation) using EXAONE Path 2.5. Integrating molecular information yields substantially improved cluster organization and enhanced separation across major anatomical and histological categories.

modalities are compared. All whole-slide images are embedded from ten CPTAC cohorts spanning nine distinct organ types. Patch-level embeddings are aggregated into slide-level representations using simple mean pooling, and the resulting latent space is visualized using t-SNE. As shown in Figure 4, embeddings learned with multimodal alignment exhibit markedly improved organ-wise clustering compared to unimodal baselines, indicating that incorporating molecular context amplifies biologically meaningful signals in histopathologic features and yields representations that better reflect underlying tissue and organ-specific phenotypes.

5 Conclusion

In this work, we introduced EXAONE Path 2.5, a pathology foundation model that bridges histopathology and multi-omics data to construct a biologically grounded representation of cancer from genotype to phenotype. By jointly modeling whole-slide images together with genomic, epigenetic, and transcriptomic modalities, our framework moves beyond morphology-only learning and captures complementary biological signals that are critical for understanding tumor behavior.

To achieve robust and efficient multimodal integration, we proposed three key design components: (1) a multimodal SigLip loss that enables all-pairwise contrastive alignment across heterogeneous modalities without inducing competition among positives, (2) a fragment-aware rotary positional encoding (F-RoPE) mechanism that preserves spatial structure and tissue-fragment topology in whole-slide images, and (3) the use of domain-specialized internal foundation models for WSI and RNA-seq to provide stable and biologically meaningful embeddings for multimodal alignment. Together, these components allow EXAONE Path 2.5 to effectively integrate diverse biological layers while remaining data- and parameter-efficient.

Extensive experiments on both internal multi-institutional clinical benchmarks and the Patho-Bench benchmark comprising 80 tasks demonstrate that EXAONE Path 2.5 achieves performance superior or on par with state-of-the-art pathology foundation models, despite being trained with substantially fewer parameters and less pretraining data. Notably, the model exhibits strong generalization across institutions and cancer types, as well as improved biological coherence in the learned representation space, as evidenced by enhanced organ- and tissue-level clustering after multimodal alignment.

Overall, our results highlight that biologically informed multimodal design can provide greater gains than scale alone in computational pathology. EXAONE Path 2.5 underscores the potential of integrated genotype-to-phenotype modeling as a foundation for next-generation precision oncology, enabling more robust molecular inference, improved clinical generalization, and deeper biological interpretability from routine histopathology data.

Table 4: Performance comparison across Patho-Bench tasks. The task column follows official Patho-Bench task names, and all models are evaluated under the same settings using linear probing. H-optimus-0 and UNI2-h use mean pooling to obtain slide-level features.

Task	CHIEF	GigaPath	PRISM	TITAN	H-optimus-0	UNI2-h	EXAONE Path 2.5
bc_therapy_er_status	0.664	0.697	0.625	0.763	0.683	0.711	0.658
bc_therapy_grade	0.743	0.654	0.722	0.781	0.731	0.751	0.720
bc_therapy_her2_status	0.644	0.646	0.718	0.729	0.711	0.678	0.735
bc_therapy_residual_cancer_burden	0.571	0.553	0.572	0.592	0.577	0.590	0.626
bcbn_er	0.872	0.895	0.893	0.919	0.928	0.912	0.914
bcbn_her2	0.722	0.719	0.718	0.749	0.747	0.747	0.708
bcbn_pr	0.815	0.814	0.821	0.836	0.858	0.851	0.847
boehmk_PFS	0.454	0.527	0.541	0.530	0.478	0.549	0.500
bracs_slidelvel_coarse	0.884	0.817	0.893	0.911	0.831	0.836	0.832
bracs_slidelvel_fine	0.834	0.765	0.839	0.850	0.786	0.793	0.793
cptac_brcancer_Immune_class	0.680	0.708	0.643	0.687	0.716	0.694	0.707
cptac_brcancer_PIK3CA_mutation	0.623	0.497	0.612	0.585	0.566	0.523	0.545
cptac_brcancer_TP53_mutation	0.820	0.740	0.853	0.838	0.748	0.766	0.762
cptac_cercc_BAP1_mutation	0.641	0.662	0.587	0.677	0.618	0.697	0.612
cptac_cercc_Immune_class	0.565	0.596	0.558	0.605	0.572	0.582	0.590
cptac_cercc_OS	0.435	0.507	0.571	0.482	0.614	0.378	0.554
cptac_cercc_PBRM1_mutation	0.470	0.481	0.504	0.528	0.447	0.473	0.454
cptac_cercc_VHL_mutation	0.561	0.602	0.462	0.522	0.486	0.459	0.524
cptac_coad_ACVR2A_mutation	0.762	0.702	0.725	0.802	0.779	0.798	0.849
cptac_coad_APP_mutation	0.613	0.713	0.694	0.748	0.702	0.722	0.781
cptac_coad_ARID1A_mutation	0.777	0.783	0.764	0.754	0.792	0.745	0.806
cptac_coad_Immune_class	0.590	0.631	0.629	0.592	0.593	0.613	0.630
cptac_coad_KRAS_mutation	0.687	0.671	0.609	0.607	0.622	0.679	0.652
cptac_coad_MSK1_H	0.844	0.849	0.859	0.875	0.885	0.884	0.933
cptac_coad_PIK3CA_mutation	0.643	0.705	0.510	0.647	0.688	0.668	0.675
cptac_coad_SETD1B_mutation	0.711	0.707	0.732	0.798	0.790	0.808	0.901
cptac_coad_TP53_mutation	0.664	0.644	0.675	0.714	0.718	0.734	0.770
cptac_gbm_EGFR_mutation	0.734	0.629	0.659	0.747	0.562	0.619	0.613
cptac_gbm_Immune_class	0.644	0.607	0.706	0.672	0.646	0.656	0.633
cptac_gbm_TP53_mutation	0.825	0.720	0.811	0.800	0.749	0.752	0.762
cptac_hnscc_CASP8_mutation	0.409	0.424	0.630	0.523	0.394	0.366	0.516
cptac_hnscc_Histologic_Grade	0.764	0.740	0.712	0.758	0.777	0.797	0.785
cptac_hnscc_Immune_class	0.626	0.595	0.712	0.612	0.620	0.614	0.623
cptac_hnscc_OS	0.565	0.664	0.599	0.578	0.678	0.599	0.738
cptac_lscc_ARID1A_mutation	0.478	0.433	0.432	0.491	0.320	0.365	0.349
cptac_lscc_Histologic_Grade	0.641	0.705	0.602	0.621	0.705	0.708	0.695
cptac_lscc_Immune_class	0.675	0.686	0.643	0.755	0.686	0.671	0.655
cptac_lscc_KEAP1_mutation	0.627	0.576	0.531	0.553	0.646	0.632	0.624
cptac_luad_EGFR_mutation	0.710	0.813	0.802	0.786	0.803	0.782	0.780
cptac_luad_Immune_class	0.720	0.632	0.660	0.697	0.625	0.613	0.644
cptac_luad_KRAS_mutation	0.630	0.743	0.682	0.742	0.759	0.699	0.723
cptac_luad_OS	0.466	0.471	0.462	0.666	0.581	0.500	0.481
cptac_luad_STK11_mutation	0.843	0.828	0.854	0.869	0.859	0.859	0.839
cptac_luad_TP53_mutation	0.672	0.687	0.718	0.740	0.678	0.731	0.634
cptac_ov_Immune_class	0.597	0.521	0.558	0.572	0.522	0.509	0.553
cptac_pda_Immune_class	0.495	0.537	0.544	0.533	0.538	0.534	0.536
cptac_pda_OS	0.546	0.454	0.590	0.591	0.490	0.457	0.505
cptac_pda_SMAD4_mutation	0.417	0.467	0.568	0.537	0.484	0.416	0.491
cptac_uecc_CTNNB1_mutation	0.714	0.748	0.718	0.713	0.756	0.748	0.767
cptac_uecc_Immune_class	0.569	0.572	0.654	0.679	0.582	0.607	0.587
cptac_uecc_PTEN_mutation	0.574	0.620	0.691	0.633	0.666	0.686	0.735
ebraains_diagnosis	0.975	0.978	0.984	0.986	0.985	0.985	0.981
ebraains_diagnosis_group	0.985	0.992	0.990	0.992	0.995	0.994	0.994
ebraains_idh_status	0.960	0.981	0.987	0.982	0.983	0.983	0.984
hancock_grading_SCC_Conventional_Keratinizing	0.725	0.683	0.651	0.722	0.702	0.722	0.717
hancock_grading_SCC_Conventional_NonKeratinizing	0.679	0.642	0.437	0.710	0.721	0.727	0.722
hancock_lymphovascular_invasion_L	0.647	0.644	0.602	0.699	0.678	0.673	0.659
hancock_OS_treatment_rdc	0.500	0.592	0.646	0.590	0.612	0.500	0.584
hancock_perineural_invasion_Pn	0.731	0.706	0.691	0.731	0.724	0.715	0.724
hancock_primarily_metastasis	0.682	0.632	0.651	0.766	0.678	0.700	0.662
hancock_primary_tumor_site	0.861	0.917	0.891	0.922	0.931	0.932	0.918
hancock_vascular_invasion_V	0.645	0.636	0.627	0.665	0.666	0.685	0.678
herroi_response	0.683	0.631	0.574	0.668	0.660	0.640	0.630
imp_grade	0.988	0.987	0.992	0.995	0.986	0.987	0.984
mbe_OS	0.575	0.508	0.508	0.631	0.495	0.443	0.507
mbe_Recist	0.635	0.588	0.616	0.642	0.598	0.604	0.630
mut-het-rcc_BAP1_mutation	0.852	0.842	0.851	0.861	0.885	0.891	0.874
mut-het-rcc_PBRM1_mutation	0.781	0.792	0.803	0.797	0.820	0.830	0.815
mut-het-rcc_SETD2_mutation	0.738	0.713	0.714	0.727	0.730	0.742	0.710
nadt_response	0.639	0.641	0.597	0.623	0.684	0.651	0.689
natbrcancer_lymphovascular_invasion	0.566	0.572	0.470	0.662	0.590	0.562	0.551
ovarian_response	0.708	0.689	0.614	0.596	0.685	0.679	0.512
panda_isup_grade	0.944	0.932	0.949	0.932	0.949	0.946	0.956
sr386_braf_mutant_binary	0.778	0.699	0.641	0.741	0.671	0.712	0.753
sr386_died_within_5_years	0.703	0.605	0.648	0.718	0.666	0.690	0.650
sr386_mmr_loss_binary	0.844	0.805	0.836	0.883	0.841	0.864	0.852
sr386_OS	0.606	0.602	0.624	0.631	0.597	0.625	0.604
sr386_ras_mutant_binary	0.696	0.605	0.625	0.691	0.627	0.678	0.683
visionmel_relapse_noprev_melanoma	0.758	0.691	0.690	0.745	0.673	0.722	0.730
visionmel_relapse_overall	0.806	0.739	0.788	0.805	0.734	0.748	0.711
AVERAGE	0.687	0.678	0.682	0.714	0.692	0.690	0.698

References

- [1] Derek C Allen. *Histopathology reporting: guidelines for surgical cancer*. Springer, 2006.
- [2] Shekoofeh Azizi, Laura Anne Culp, Jan Freyberg, Basil Mustafa, Sebastien Baur, Simon Kornblith, Ting Chen, Patricia MacWilliams, Sara Mahdavi, Ellery Wulczyn, Boris Babenko, Megan Zoë Walker, Aaron Loh, Cameron Chen, Yuan Liu, Pinal Bavishi, Scott Mayer McKinney, Jim Winkens, Abhijit Guha Roy, Zach William Beaver, Fiona Keleher Ryan, Justin David Krogue, Mozziyar Etemadi, Umesh Telang, Yun Liu, Lily Hao Yi Peng, Greg Corrado, Dale Richard Webster, David James Fleet, Geoffrey Everest Hinton, Neil Houlsby, Alan Karthikesalingam, Mohammad Norouzi, and Vivek Natarajan. Robust and data-efficient generalization of self-supervised machine learning for diagnostic imaging. *Nature Biomedical Engineering*, 2023.
- [3] Gabriele Campanella, Ricky Kwan, Eugene Fluder, Jennifer Zeng, Aryeh Stock, Brandon Veremis, Alexandros D Polydorides, Cyrus Hedvat, Adam Schoenfeld, Chad Vanderbilt, et al. Computational pathology at health system scale—self-supervised foundation models from three billion images. *arXiv preprint arXiv:2310.07033*, 2023.
- [4] Richard J Chen, Chengkuan Chen, Yicong Li, Tiffany Y Chen, Andrew D Trister, Rahul G Krishnan, and Faisal Mahmood. Scaling vision transformers to gigapixel images via hierarchical self-supervised learning. In *Proceedings of the IEEE/CVF Conference on Computer Vision and Pattern Recognition*, pages 16144–16155, 2022.
- [5] Richard J Chen, Tong Ding, Ming Y Lu, Drew FK Williamson, Guillaume Jaume, Bowen Chen, Andrew Zhang, Daniel Shao, Andrew H Song, Muhammad Shaban, et al. Towards a general-purpose foundation model for computational pathology. *Nature Medicine*, 2024.
- [6] Tong Ding, Sophia J Wagner, Andrew H Song, Richard J Chen, Ming Y Lu, Andrew Zhang, Anurag J Vaidya, Guillaume Jaume, Muhammad Shaban, Ahrong Kim, et al. Multimodal whole slide foundation model for pathology. *arXiv preprint arXiv:2411.19666*, 2024.
- [7] Mengmeng Dong, Liping Wang, Ning Hu, Yueli Rao, Zhen Wang, and Yu Zhang. Integration of multi-omics approaches in exploring intra-tumoral heterogeneity. *Cancer Cell International*, 25(1):317, 2025.
- [8] Alexandre Filiot, Ridouane Ghermi, Antoine Olivier, Paul Jacob, Lucas Fidon, Alice Mac Kain, Charlie Saillard, and Jean-Baptiste Schiratti. Scaling self-supervised learning for histopathology with masked image modeling. *medRxiv*, pages 2023–07, 2023.
- [9] Douglas Hanahan and Robert A Weinberg. Hallmarks of cancer: the next generation. *cell*, 144(5):646–674, 2011.
- [10] Yong Jin Heo, Chanwoong Hwa, Gang-Hee Lee, Jae-Min Park, and Joon-Yong An. Integrative multi-omics approaches in cancer research: from biological networks to clinical subtypes. *Molecules and cells*, 44(7):433–443, 2021.
- [11] Maximilian Ilse, Jakub Tomczak, and Max Welling. Attention-based deep multiple instance learning. In *International conference on machine learning*, pages 2127–2136. PMLR, 2018.
- [12] Alex Ing, Alvaro Andrades, Marco Raffaele Cosenza, and Jan O Korbel. Integrating multimodal cancer data using deep latent variable path modelling. *Nature Machine Intelligence*, 7(7):1053–1075, 2025.
- [13] Andrew Jaegle, Felix Gimeno, Andy Brock, Oriol Vinyals, Andrew Zisserman, and Joao Carreira. Perceiver: General perception with iterative attention. In *International conference on machine learning*, pages 4651–4664. PMLR, 2021.
- [14] Lokesh Jain, Craig A Vargo, Romano Danesi, Tristan M Sissung, Douglas K Price, David Venzon, Jürgen Venitz, and William D Figg. The role of vascular endothelial growth factor snps as predictive and prognostic markers for major solid tumors. *Molecular cancer therapeutics*, 8(9):2496–2508, 2009.
- [15] Guillaume Jaume, Lukas Oldenburg, Anurag Vaidya, Richard J Chen, Drew FK Williamson, Thomas Peeters, Andrew H Song, and Faisal Mahmood. Transcriptomics-guided slide representation learning in computational pathology. In *Proceedings of the IEEE/CVF Conference on Computer Vision and Pattern Recognition*, pages 9632–9644, 2024.

[16] Mingu Kang, Heon Song, Seonwook Park, Donggeun Yoo, and Sérgio Pereira. Benchmarking self-supervised learning on diverse pathology datasets. In *Proceedings of the IEEE/CVF Conference on Computer Vision and Pattern Recognition*, pages 3344–3354, 2023.

[17] Mahendra Khened, Avinash Kori, Haran Rajkumar, Ganapathy Krishnamurthi, and Balaji Srinivasan. A generalized deep learning framework for whole-slide image segmentation and analysis. *Scientific reports*, 11(1):11579, 2021.

[18] Marta Kulis and Manel Esteller. Dna methylation and cancer. *Advances in genetics*, 70:27–56, 2010.

[19] Ming Y Lu, Drew FK Williamson, Tiffany Y Chen, Richard J Chen, Matteo Barbieri, and Faisal Mahmood. Data-efficient and weakly supervised computational pathology on whole-slide images. *Nature biomedical engineering*, 5(6):555–570, 2021.

[20] Maxime Oquab, Timothée Darzet, Théo Moutakanni, Huy Vo, Marc Szafraniec, Vasil Khalidov, Pierre Fernandez, Daniel Haziza, Francisco Massa, Alaaeldin El-Nouby, et al. Dinov2: Learning robust visual features without supervision. *arXiv preprint arXiv:2304.07193*, 2023.

[21] Myeongjang Pyeon, Janghyeon Lee, Minsoo Lee, Juseung Yun, Hwanil Choi, Jonghyun Kim, Jiwon Kim, Yi Hu, Jongseong Jang, and Soonyoung Lee. Exaone path 2.0: Pathology foundation model with end-to-end supervision. *arXiv preprint arXiv:2507.06639*, 2025.

[22] Aharon Razin and Howard Cedar. Dna methylation and gene expression. *Microbiological reviews*, 55(3):451–458, 1991.

[23] George Shaikovski, Adam Casson, Kristen Severson, Eric Zimmermann, Yi Kan Wang, Jeremy D Kunz, Juan A Retamero, Gerard Oakley, David Klimstra, Christopher Kanan, et al. Prism: A multi-modal generative foundation model for slide-level histopathology. *arXiv preprint arXiv:2405.10254*, 2024.

[24] Carol L Shields, Hong Sun, Hakan Demirci, and Jerry A Shields. Factors predictive of tumor growth, tumor decalcification, choroidal neovascularization, and visual outcome in 74 eyes with choroidal osteoma. *Archives of Ophthalmology*, 123(12):1658–1666, 2005.

[25] Jianlin Su, Murtadha Ahmed, Yu Lu, Shengfeng Pan, Wen Bo, and Yunfeng Liu. Roformer: Enhanced transformer with rotary position embedding. *Neurocomputing*, 568:127063, 2024.

[26] Anurag Vaidya, Andrew Zhang, Guillaume Jaume, Andrew H Song, Tong Ding, Sophia J Wagner, Ming Y Lu, Paul Doucet, Harry Robertson, Cristina Almagro-Perez, et al. Molecular-driven foundation model for oncologic pathology. *arXiv preprint arXiv:2501.16652*, 2025.

[27] Eugene Vorontsov, Alican Bozkurt, Adam Casson, George Shaikovski, Michal Zelechowski, Siqi Liu, Philippe Mathieu, Alexander van Eck, Donghun Lee, Julian Viret, et al. Virchow: a million-slide digital pathology foundation model. *arXiv preprint arXiv:2309.07778*, 2023.

[28] Xiyue Wang, Sen Yang, Jun Zhang, Minghui Wang, Jing Zhang, Wei Yang, Junzhou Huang, and Xiao Han. Transformer-based unsupervised contrastive learning for histopathological image classification. *Medical image analysis*, 81:102559, 2022.

[29] Xiyue Wang, Junhan Zhao, Eliana Marostica, Wei Yuan, Jietian Jin, Jiayu Zhang, Ruijiang Li, Hongping Tang, Kanran Wang, Yu Li, et al. A pathology foundation model for cancer diagnosis and prognosis prediction. *Nature*, 634(8035):970–978, 2024.

[30] Hanwen Xu, Naoto Usuyama, Jaspreet Bagga, Sheng Zhang, Rajesh Rao, Tristan Naumann, Cliff Wong, Zelalem Gero, Javier González, Yu Gu, Yanbo Xu, Mu Wei, Wenhui Wang, Shuming Ma, Furu Wei, Jianwei Yang, Chunyuan Li, Jianfeng Gao, Jaylen Rosemon, Tucker Bower, Soohee Lee, Roshanthy Weersasinghe, Bill J. Wright, Ari Robicsek, Brian Piening, Carlo Bifulco, Sheng Wang, and Hoifung Poon. A whole-slide foundation model for digital pathology from real-world data. *Nature*, 2024.

[31] Xiaohua Zhai, Basil Mustafa, Alexander Kolesnikov, and Lucas Beyer. Sigmoid loss for language image pre-training. In *Proceedings of the IEEE/CVF international conference on computer vision*, pages 11975–11986, 2023.

EXAONEPath AI Model License Agreement 1.0 - NC

This License Agreement (“Agreement”) is entered into between you (“Licensee”) and LG Management Development Institute Co., Ltd. (“Licensor”), governing the use of the EXAONEPath AI Model (“Model”). By downloading, installing, copying, or using the Model, you agree to comply with and be bound by the terms of this Agreement. If you do not agree to all the terms, you must not download, install, copy, or use the Model. This Agreement constitutes a binding legal agreement between the Licensee and Licensor.

1. Definitions

1.1 Model

The artificial intelligence model provided by Licensor, which includes any software, algorithms, machine learning models, or related components supplied by Licensor. This definition extends to encompass all updates, enhancements, improvements, bug fixes, patches, or other modifications that may be provided by Licensor from time to time, whether automatically or manually implemented.

1.2 Derivatives

Any modifications, alterations, enhancements, improvements, adaptations, or derivative works of the Model created by Licensee or any third party. This includes changes made to the Model’s architecture, parameters, data processing methods, or any other aspect of the Model that results in a modification of its functionality or output.

1.3 Output

Any data, results, content, predictions, analyses, insights, or other materials generated by the Model or Derivatives, regardless of whether they are in their original form or have been further processed or modified by the Licensee. This includes, but is not limited to, textual or numerical produced directly or indirectly through the use of the Model.

1.4 Licensor

LG Management Development Institute Co., Ltd., the owner, developer, and provider of the EXAONEPath AI Model. The Licensor holds all rights, title, and interest in the Model and is responsible for granting licenses to use the Model under the terms specified in this Agreement.

1.5 Licensee

The individual, organization, corporation, academic institution, government agency, or other entity using or intending to use the Model under the terms and conditions of this Agreement. The Licensee is responsible for ensuring compliance with the Agreement by all authorized users who access or utilize the Model on behalf of the Licensee.

2. License Grant

2.1 Grant of License

Subject to the terms and conditions outlined in this Agreement, the Licensor hereby grants the Licensee a limited, non-exclusive, non-transferable, worldwide, and revocable license to:

- a. Access, download, install, and use the Model solely for research purposes. This includes evaluation, testing, academic research and experimentation.
- b. Publicly disclose research results and findings derived from the use of the Model or Derivatives, including publishing papers or presentations.

- c. Modify the Model and create Derivatives based on the Model, provided that such modifications and Derivatives are used exclusively for research purposes. The Licensee may conduct experiments, perform analyses, and apply custom modifications to the Model to explore its capabilities and performance under various scenarios. If the Model is modified, the modified Model must include "EXAONEPath" at the beginning of its name.
- d. Distribute the Model and Derivatives in each case with a copy of this Agreement.

2.2 Scope of License

The license granted herein does not authorize the Licensee to use the Model for any purpose not explicitly permitted under this Agreement. Any use beyond the scope of this license, including any commercial application or external distribution, is strictly prohibited unless explicitly agreed upon in writing by the Licenser.

3. Restrictions

3.1 Commercial Use

The Licensee is expressly prohibited from using the Model, Derivatives, or Output for any commercial purposes, including but not limited to, developing or deploying products, services, or applications that generate revenue, whether directly or indirectly. Any commercial exploitation of the Model or its derivatives requires a separate commercial license agreement with the Licenser. Furthermore, the Licensee shall not use the Model, Derivatives or Output to develop or improve other models, except for research purposes, which is explicitly permitted.

3.2 Reverse Engineering

The Licensee shall not decompile, disassemble, reverse engineer, or attempt to derive the source code, underlying ideas, algorithms, or structure of the Model, except to the extent that such activities are expressly permitted by applicable law. Any attempt to bypass or circumvent technological protection measures applied to the Model is strictly prohibited.

3.3 Unlawful Use

The Licensee shall not use the Model and Derivatives for any illegal, fraudulent, or unauthorized activities, nor for any purpose that violates applicable laws or regulations. This includes but is not limited to the creation, distribution, or dissemination of malicious, deceptive, or unlawful content.

3.4 Ethical Use

The Licensee shall ensure that the Model or Derivatives is used in an ethical and responsible manner, adhering to the following guidelines:

- a. The Model and Derivatives shall not be used to generate, propagate, or amplify false, misleading, or harmful information, including fake news, misinformation, or disinformation.
- b. The Model and Derivatives shall not be employed to create, distribute, or promote content that is discriminatory, harassing, defamatory, abusive, or otherwise offensive to individuals or groups based on race, gender, sexual orientation, religion, nationality, or other protected characteristics.
- c. The Model and Derivatives shall not infringe on the rights of others, including intellectual property rights, privacy rights, or any other rights recognized by law. The Licensee shall obtain all necessary permissions and consents before using the Model and Derivatives in a manner that may impact the rights of third parties.
- d. The Model and Derivatives shall not be used in a way that causes harm, whether physical, mental, emotional, or financial, to individuals, organizations, or communities. The Licensee shall take all reasonable measures to prevent misuse or abuse of the Model and Derivatives that could result in harm or injury.

4. Ownership

4.1 Intellectual Property

All rights, title, and interest in and to the Model, including any modifications, Derivatives, and associated documentation, are and shall remain the exclusive property of the Licensor. The Licensee acknowledges that this Agreement does not transfer any ownership rights to the Licensee. All trademarks, service marks, and logos associated with the Model are the property of the Licensor.

4.2 Output

All output generated by the Model from Licensee Data ("Output") shall be the sole property of the Licensee. Licensor hereby waives any claim of ownership or intellectual property rights to the Output. Licensee is solely responsible for the legality, accuracy, quality, integrity, and use of the Output.

4.3 Attribution

In any publication or presentation of results obtained using the Model, the Licensee shall provide appropriate attribution to the Licensor, citing the Model's name and version, along with any relevant documentation or references specified by the Licensor.

5. No Warranty

5.1 "As-Is" Basis

The Model, Derivatives, and Output are provided on an "as-is" and "as-available" basis, without any warranties or representations of any kind, whether express, implied, or statutory. The Licensor disclaims all warranties, including but not limited to, implied warranties of merchantability, fitness for a particular purpose, accuracy, reliability, non-infringement, or any warranty arising from the course of dealing or usage of trade.

5.2 Performance and Reliability

The Licensor does not warrant or guarantee that the Model, Derivatives or Output will meet the Licensee's requirements, that the operation of the Model, Derivatives or Output will be uninterrupted or error-free, or that defects in the Model will be corrected. The Licensee acknowledges that the use of the Model, Derivatives or Output is at its own risk and that the Model, Derivatives or Output may contain bugs, errors, or other limitations.

5.3 No Endorsement

The Licensor does not endorse, approve, or certify any results, conclusions, or recommendations derived from the use of the Model. The Licensee is solely responsible for evaluating the accuracy, reliability, and suitability of the Model for its intended purposes.

6. Limitation of Liability

6.1 No Liability for Damages

To the fullest extent permitted by applicable law, in no event shall the Licensor be liable for any special, incidental, indirect, consequential, exemplary, or punitive damages, including but not limited to, damages for loss of business profits, business interruption, loss of business information, loss of data, or any other pecuniary or non-pecuniary loss arising out of or in connection with the use or inability to use the Model, Derivatives or any Output, even if the Licensor has been advised of the possibility of such damages.

6.2 Indemnification

The Licensee agrees to indemnify, defend, and hold harmless the Licensor, its affiliates, officers, directors, employees, and agents from and against any claims, liabilities, damages, losses, costs, or expenses (including reasonable attorneys' fees) arising out of or related to the Licensee's use of the Model, any Derivatives, or any Output, including any violation of this Agreement or applicable laws. This includes, but is not limited to, ensuring compliance with copyright laws, privacy regulations, defamation laws, and any other applicable legal or regulatory requirements.

7. Termination

7.1 Termination by Licensor

The Licensor reserves the right to terminate this Agreement and revoke the Licensee's rights to use the Model at any time, with or without cause, and without prior notice if the Licensee breaches any of the terms or conditions of this Agreement. Termination shall be effective immediately upon notice.

7.2 Effect of Termination

Upon termination of this Agreement, the Licensee must immediately cease all use of the Model, Derivatives, and Output and destroy all copies of the Model, Derivatives, and Output in its possession or control, including any backup or archival copies. The Licensee shall certify in writing to the Licensor that such destruction has been completed.

7.3 Survival

The provisions of this Agreement that by their nature should survive termination, including but not limited to, Sections 4 (Ownership), 5 (No Warranty), 6 (Limitation of Liability), and this Section 7 (Termination), shall continue to apply after termination.

8. Governing Law

8.1 Governing Law

This Agreement shall be governed by and construed in accordance with the laws of the Republic of Korea, without regard to its conflict of laws principles.

8.2 Arbitration

Any disputes, controversies, or claims arising out of or relating to this Agreement, including its existence, validity, interpretation, performance, breach, or termination, shall be referred to and finally resolved by arbitration administered by the Korean Commercial Arbitration Board (KCAB) in accordance with the International Arbitration Rules of the Korean Commercial Arbitration Board in force at the time of the commencement of the arbitration. The seat of arbitration shall be Seoul, Republic of Korea. The tribunal shall consist of one arbitrator. The language of the arbitration shall be English.

9. Alterations

9.1 Modifications

The Licensor reserves the right to modify or amend this Agreement at any time, in its sole discretion. Any modifications will be effective upon posting the updated Agreement on the Licensor's website or through other means of communication. The Licensee is responsible for reviewing the Agreement periodically for changes. Continued use of the Model after any modifications have been made constitutes acceptance of the revised Agreement.

9.2 Entire Agreement

This Agreement constitutes the entire agreement between the Licensee and Licensor concerning the subject matter hereof and supersedes all prior or contemporaneous oral or written agreements, representations, or understandings. Any terms or conditions of any purchase order or other document submitted by the Licensee in connection with the Model that are in addition to, different from, or inconsistent with the terms and conditions of this Agreement are not binding on the Licensor and are void.

By downloading, installing, or using the EXAONEPath AI Model, the Licensee acknowledges that it has read, understood, and agrees to be bound by the terms and conditions of this Agreement.